ELSEVIER

Ceramics International 26 (2000) 397–410

CERAMICS INTERNATIONAL

Microstructure dependent hardness and fracture behavior in liquid-phase-sintered Al_2O_3

Amiya P. Goswami [a,*], Sukumar Roy [a], Manoj K. Mitra [b], Gopes C. Das [b]

[a] *Ceramic Technological Institute, Bharat Heavy Electricals Limited, Bangalore 560 012, India*
[b] *Department of Metallurgical Engineering, Jadavpur University, Calcutta 700 032, India*

Received 22 March 1999; received in revised form 15 May 1999; accepted 1 July 1999

Abstract

The liquid-phase-sintered Al_2O_3 (LPS) derived from commercial powders of different particle size, e.g. coarse (70–100 μm), medium (3.6–7.0 μm) and reactive (< 2.0 μm) showed a substantial differences in Vickers indentation fracture behavior depending upon their grain size distribution and thermal expansion coefficient mismatch between the matrix grain and the intergranular phases. A high true hardness and a low indentation crack length was observed in the case of the LPS with reactive powder which was attributed due to enhanced dissolution of Al_2O_3 into the glassy phase. A high flexural strength was achieved with the LPS of medium powder. A high $K_{ic\text{-}short}$ always resulted either due to (i) the MgO/(CaO + BaO + KNaO) ratio of nearly 1 in the chemical composition of LPS, or (ii) higher modulus of elasticity to hardness ratio, or (iii) reinforcement of coarse grains (> 12 μm) in the fine-grained (~2 μm) microstructure. The crack path was predominantly intergranular at lower MgO/(CaO + BaO + KNaO) ratio (< 1.0) for the indentation load in between 9.81 and 49.03 N, whereas it was transgranular at a higher ratio (~1.6). A low $K_{ic\text{-}short}$ was observed due to precipitation of anorthite phase in the LPS with a high MgO/(CaO + BaO + KNaO) ratio. Finally the sintered density of 91–94 wt% LPS materials comprising of all powders produced a linear relationship with both the hardness and the modulus of elasticity.

Keywords: C. Hardness; C. Mechanical properties; C. Toughness and toughening; D. Alkaline earth oxides; D. Alkali oxides; D. Al_2O_3

1. Introduction

Hardness and fracture toughness have been extensively applied in modeling functional characteristics like strength, wear, and machining and ballistic performance [1,2]. Convenience in measurement of these parameters by a simple indentation technique [3] has been the motivating factor for the material researchers to explore further. Liquid-phase-sintered (LPS) Al_2O_3 are well known for a better suitability over glass-free polycrystalline Al_2O_3 in many applications despite their low hardness, macroscopic fracture toughness and mechanical strength [4].

The hardness (H) of a brittle material, as evaluated by conventional tests (Vickers, Knoop, Berkovich, etc.), is a measure of a material's resistance to deformation, densification, displacement and fracture. The grain size (G) though related [5,6] to H linearly by $H\alpha G^{-1/2}$, has been found to have exceptions at low loads (< 200 g) following the Meyer's law, $P = Cd^n$, where P is the load, d is the measured size of the impression and C is a constant. A hardness minima has been reported when the indentation size correspond to the grain size [5] in the microstructure.

Braun et al. [7] showed the advantages of the indentation method ($K_{ic\text{-}short}$) over the conventional notched beam specimen ($K_{ic\text{-}long}$) for investigation of fracture toughness (T-curves, K_R-curves or R-curves) on the basis of the short crack flaw of the order of microstructural defect size. The flaw tolerance has been shown to be enhanced in Al_2O_3 by bridging either (i) with a higher grain size or (ii) with a second phase e.g. calcium hexaluminate/anorthite/Al_2TiO_5 at the grain boundary [8–11]. Besides the grain-size, the microstructural features like grain morphology, grain boundary phases, porosity and also thermal history are believed to have a significant influence on the mechanical properties.

* Corresponding author. Tel.: +91-80-334-6392; fax: +91-80-334-4231.
E-mail address: apgoswami@vsnl.com (A.P. Goswami).

0272-8842/00/$20.00
PII: S0272-8842(99)00070-X

Toughening mechanisms like crack bowing, crack deflection, microcracking and crack front debonding have also been reported in ceramics and ceramic composites [12–14].

The degree of crystallinity from the intergranular glassy phase of commercial LPS Al_2O_3 was shown [15–17] to have relatively little or no effect on the mechanical properties. In these studies, the changes of the grain shape and size in the microstructure were reported to be insignificant. In our previous work [18], the differences in the morphology of 89–94 wt% LPS Al_2O_3 materials prepared in the laboratory using medium and coarse grade powders were reported. The formation of elongated grains (aspect ratio greater than 2.1) was favored when the concentration of MgO was relatively low over the concentration of alkali and alkaline earth oxides. It was shown that MgO/(CaO + BaO + KNaO) ratio and SiO_2 content in the chemical composition controlled the morphology and grain size distribution. As expected, the thermal expansion mismatch stresses in the grain boundary region also changed simultaneously due to the differences in the thermal expansion of the glassy phase [19].

In this article, the role of morphology, grain size distribution and intergranular phases in the microstructure of LPS containing 89–97 wt% Al_2O_3 derived from different powders of commercial sources will be reported. Hardness and the indentation fracture toughness have been measured over a wide range of load in order to understand the load dependent behavior. The nature of crack formed at the indentation site will be co-related with the microstructural features of different LPS materials. An attempt will also be made to establish the interrelationship between the mechanical properties.

2. Experimental

Different LPS materials with Al_2O_3 content of 89–97 wt% were prepared using powders of different particle size — coarse (70–100 μm), medium (3.6–7.0 μm), reactive (< 2.0 μm). In the coarse variety, two grades, i.e. 'M' and 'S', were used. Likewise, 'I' and 'O' were the grades in medium variety and 'R' and 'A16' in reactive variety. Usage of different sintering additives produced different phases in the grain boundary region with the constituents, e.g. K_2O, Na_2O, CaO, BaO, MgO and SiO_2.

91–94 wt% Al_2O_3 LPS materials have been classified into three categories, i.e. A, B and C with a view to differentiate between the microstructure and internal thermal expansion and modulus of elasticity mismatch stresses. The materials with MgO/(CaO + BaO + KNaO) ratio < 1.0 are named 'A' type, ratio between 1.0 and 1.5 as 'B' type and between 1.5 and 2.0 as 'C' type. The materials of 95–97 wt% Al_2O_3 have been named 'H' type and that of the 88–90 wt% as 'D' type. For easy identification, a suffix has been assigned to each of the compositions, which denotes the grade of the powder used in that composition.

Specimens were fabricated using uniaxial powder compaction technique and sintered in normal air pressure. Specimens of 91–97% of theoretical density with negligible open porosity (< 0.25%) were used in the study along with few samples from commercial sources ($A5_o$ and C5).

An image analyzer with software was employed to carry out the morphological analysis. Details of material selection, powder preparation, chemical composition of the sintered specimens, microstructural characterization like grain size, morphology and the relative amount of different intergranular phases present in the sintered specimen were characterized and reported elsewhere [18,20].

Specimens for hardness and indentation fracture toughness were cut from the bulk and subsequently polished using diamond paste starting with coarse (2–3 μm) grits and then down to 1 μm until an optically reflecting surface was achieved. Hardness was measured with Shimadzu's HSV2000 model hardness tester using a Knoop indentor. The peak loads for the indentations were in the range of 1.96–98.07 N, which was applied for a duration of 15 s under constant loading/unloading speed. True hardness, H_o, has been calculated from the equation [21]

$$d = (14229/H_o)^{1/2} P^{1/2} - d_e \quad (1)$$

where d_e is the correction factor for elastic deformation. The slope of the equation in (1) was obtained from the regression analysis using an average of minimum 10 readings in 'd' at each load. However the maximum load considered for the determination of true hardness was limited to 9.81 N so as to avoid the effect of crack formation at higher loads except in $C7_{A16}$ where it was upto 24.52 N. The appearance of very small cracks, however, was ignored.

Fracture toughness ($K_{ic\text{-}short}$) was measured from the crack length formed by Vickers indentation at the same load interval and duration as that of the hardness test. A minimum of 10 readings was taken at each load upto 9.81 N and five readings at higher loads. The crack length was measured within 30 s. A magnification of 500x attached with the hardness tester was used for the measurement of the crack length. The profile of the crack was recorded for each indentation at different loads. The tests were carried out at room temperature and with ~50% relative humidity in the atmosphere. Indentations with extensive multiple cracks from the corners or from the sides or that of the one containing chipping were rejected. Parallelity in the specimen was maintained sufficiently so as to get a uniform shape of the indentation. Thermally etched (with cooling rate of

sintering) specimen was used to investigate fracture path in SEM (Leica S440).

Flexural strength was measured by three-point bend test method at a load rate of 35 N/s. Modulus of elasticity was tested by sonic method as per ASTM procedure [22].

3. Results and discussion

3.1. Microstructure

The SEM images explaining the morphological changes in the sintered sample have been presented elsewhere [18,20]. Some of the related features are mentioned here briefly. 'A' type LPS prepared from coarse and medium powders had elongated grains with aspect ratio (average of major/minor axis) >2.1 while both the 'B' and 'C' type had equiaxed grains with the aspect ratio ~ 2.0. Further, the elongation of the grains in these materials was also favored when SiO_2 content was low (3.88 wt% in $A6_M$ and 3.83 wt% in $B6_I$). Fig. 1 shows the TEM images of $A1_I$ and $B7_I$ materials containing 92.13 and 91.78 wt% of Al_2O_3 and with $MgO/(CaO + BaO + KNaO)$ ratio of 0.41 and 1.31, respectively. The images show the distribution of glassy phase and the triple point junctions while indicating the morphological changes in the Al_2O_3 grains occurred during sintering. Vol% of glass and pore, as measured by the 'point count' method, has been found to be 21 and 9, respectively, for a 91–94% Al_2O_3 LPS material such as B7I typically. The LPS materials derived from the reactive powders have equiaxed morphology as seen from Fig. 1(c). The micrographs of 95–97% materials from the reactive powders as well as coarse powder had equiaxed grains as represented in Fig. 1(d). Table 1 shows the grain size analyses of certain selective LPS Al_2O_3 comprising of all varieties of powders and Al_2O_3 content.

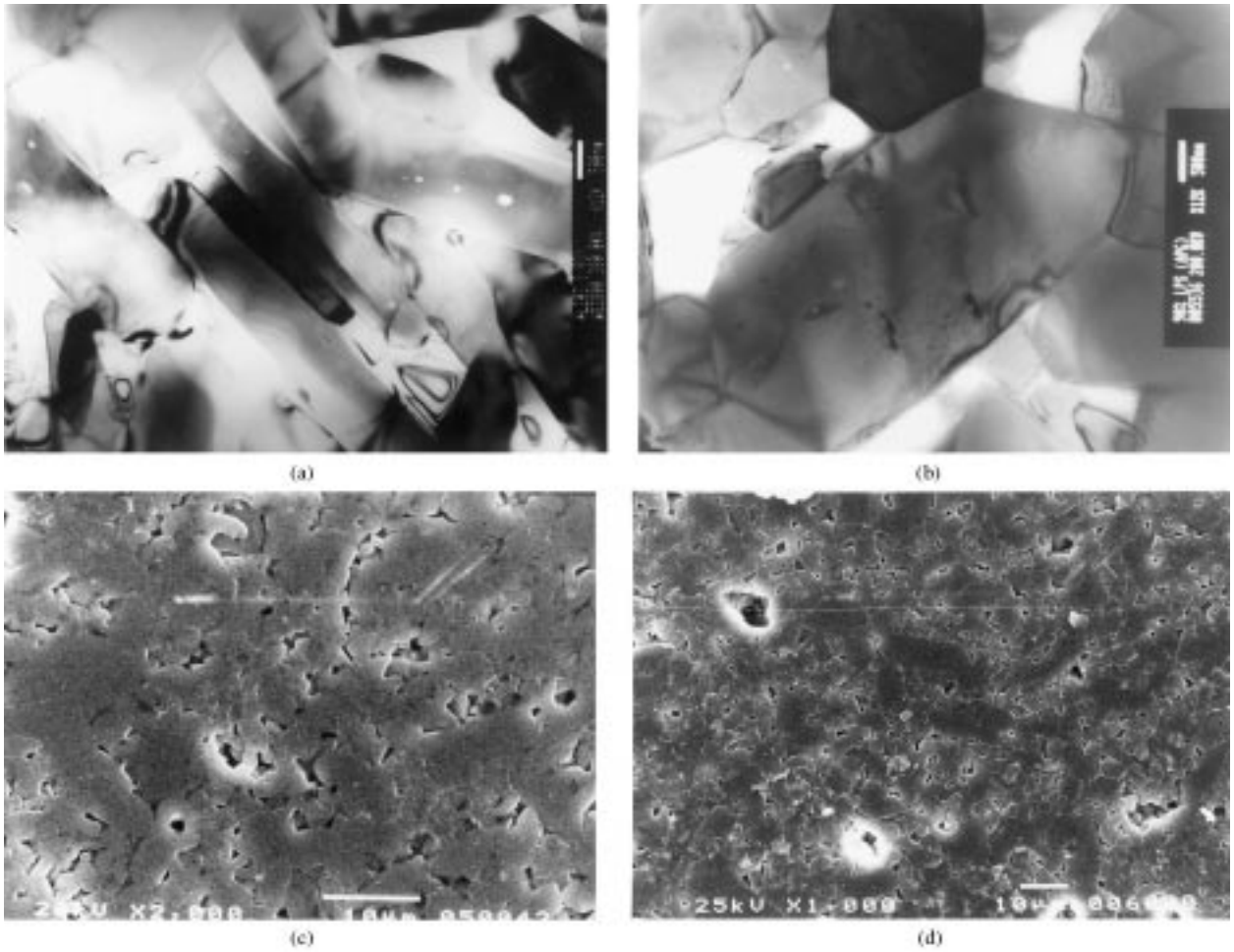

Fig. 1. Microstructure of LPS Al_2O_3 ceramics showing the differences in the morphology in (a) $A1_I$, (b) $B7_I$, (c) $A7_R$ and (d) $H3_{A16}$ (aspect ratio and Feret dia. of 2.34 and 1.93 μm in $A1_I$ and 1.99 and 2.81 μm in $B7_I$).

3.2. Mechanical properties

Fig. 2 represents the length of the crack from the corner of an indentation, $l(=c-d/2)$, in log scale against the applied load for various LPS materials. As can be seen that the crack length is lower in the case of those LPS derived from the reactive powders with a nearly identical composition (compare $A8_R$ with $A1_I$, $C7_{A16}$ with $C1_I$ and $C2_S$ and $H3_R$ with $H6_S$). The same figure also implies (by converting ordinate to linear scale) that the crack length follows a linear relationship with the applied load. The square of correlation coefficient (r^2) has been found to be greater than 0.91 for all the materials except in $D2_S$ where it is as low as 0.73 due to a reduction in crack length at 49.03 N load. The absence of a characteristic knee shows that the crack is radial type and not in the Palmqvist regime. $K_{ic\text{-}short}$ has been obtained from the following formula:

$$K_{ic\text{-}short} = 0.018(E/H_0)^{1/2}P/c^{3/2} \quad (2)$$

where c is the crack length as defined elsewhere [21]. The values of $K_{ic\text{-}short}$ have been found to be comparable with the values of $K_{ic\text{-}long}$ obtained from 'single edge notched beam' test (SENB) carried out with 1.50 mm of notched depth and at a crosshead speed of 0.5 mm/min. Results of $K_{ic\text{-}short}$ and $K_{ic\text{-}long}$ are seen in Table 2. Table 3 shows the results of E, H_o and flexural strength along with the related microstructural parameters like the maximum size of the grains and voids observed in the polished and etched specimen.

Table 1
Grain size analysis and aspect ratio of certain LPS Al_2O_3 ceramics[a]

Material code	Aspect ratio	Feret dia.		Major axis		Minor axis	
		$\bar{X}$	σ	$\bar{X}$	σ	$\bar{X}$	σ
$A5_o$	2.2	4.2	2.62	6.5	4.66	3.0	2.32
$A7_R$	1.9	2.3	1.08	3.3	1.82	1.8	0.97
$A8_R$	1.8	2.4	1.78	3.4	3.17	1.9	1.65
$C1_I$	2.1	2.0	1.09	3.1	1.87	1.5	0.97
$C2_S$iv	1.9	2.9	2.96	4.7	4.48	2.5	2.48
$C6_R$	2.1	1.4	0.96	2.1	1.69	1.0	0.78
$C7_{A16}$	2.0	1.0	0.59	1.5	1.45	0.7	0.51
$H6_S$	1.8	3.5	1.85	4.7	2.84	2.6	1.88
$H3_{A16}$	1.8	2.6	1.90	3.7	3.05	2.;1	1.74
$H3_R$	1.9	1.8	1.17	2.6	1.92	1.4	1.02

[a] Dimension in μm.

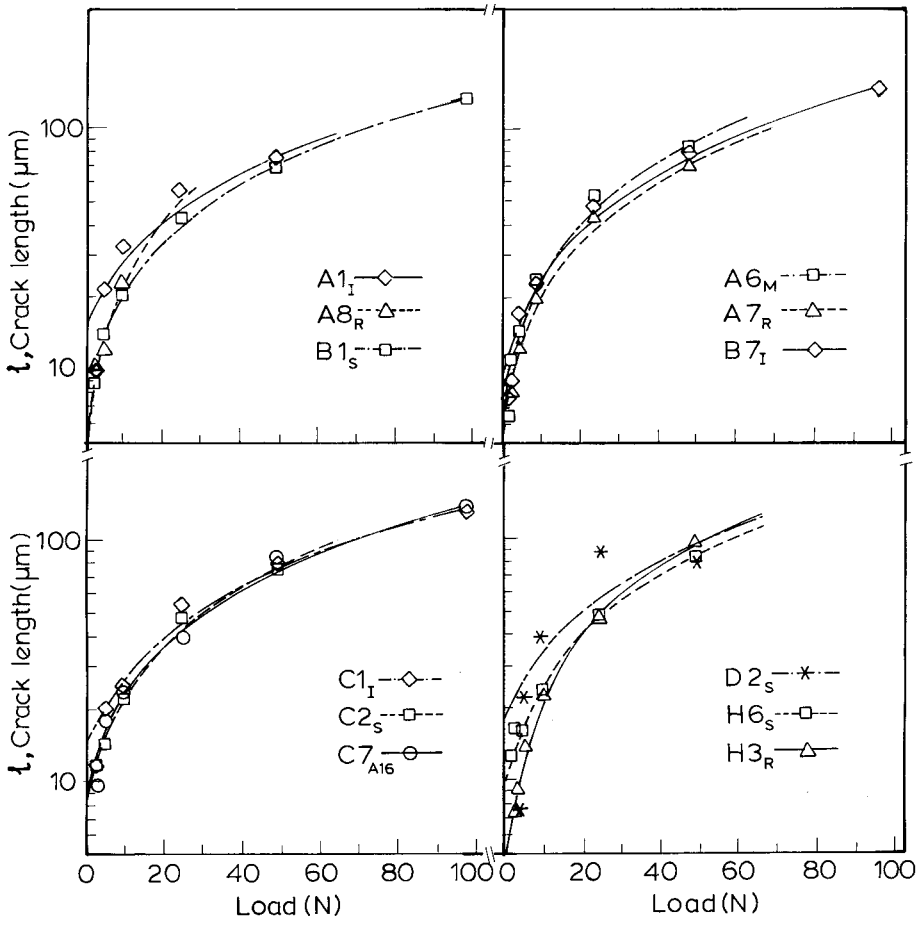

Fig. 2. Indentation load versus crack length, l, for different LPS Al_2O_3 derived from different powders, e.g. 1. coarse (Malco*) □, 2. coarse (Indal*) □ and ∗, 3. medium (Indal) ◇, 4. MROI grade (Indal) △, 5. A16SG (Alcoa), USA. ○. $l=c$-$d/2$. *Indian sources.

Table 2
Fracture toughness by indentation and SENB method in LPS Al_2O_3 ceramics

Material code	Load (N)	d (μm)	Hv (GPa)	K_{ic} (MPa $m^{1/2}$)	Std. dev. of K_{ic}	% OK crack system	Nature of cracks
$A1_I$	2.94	23.45	10.04	2.84	0.226	75	Multiple cracks and bowing
	4.90	29.82	10.25	2.23	0.345	60	Multiple cracks and bowing
	9.81	43.02	9.87	2.48	0.389	90	Zigzag and branched
	24.52	70.69	9.10	2.75	0.180	75	Branched and multiple cracks
	49.03	95.43	10.00	3.71	0.420	100	Bridged with extra cracks
$A2_M$	2.94	22.20	11.09	2.64	–	20	Zigzag and multiple cracks
	4.90	28.27	11.53	2.57	0.314	75	Zigzag and multiple cracks
	9.81	41.38	10.68	2.47	0.183	82	Zigzag and multiple cracks
$A5_o$	2.94	21.57	11.74	2.68	–	67	Multiple cracks and bowing
	4.90	30.78	9.91	2.71	0.299	100	Chipping and zigzag cracks
	9.81	40.27	11.35	2.42	0.599	100	Chipping, bowing/zigzag crack
$A6_M$	1.96	16.35	13.63	3.33	0.358	60	Improper cracks and chipping
	2.94	20.14	13.53	2.95	0.445	40	Chipping and multiple cracks
	4.90	26.36	13.11	3.33	0.477	67	Zigzag and multiple crack
	9.81	38.63	12.20	3.47	0.407	90	Multiple cracks
	24.52	62.19	11.76	3.25	0.351	67	Zigzag and multiple crack
	49.03	87.35	11.92	3.40	0.241	100	Bridged with extra cracks
$B1_S$	2.94	22.10	11.28	2.97	0.290	82	Fairly straight crack and bowing
	4.90	28.22	11.44	2.98	0.435	90	Fairly straight crack and bowing
	9.81	41.78	10.46	3.30	0.361	80	Straight and multiple crack
	24.52	64.49	10.94	3.40	0.315	90	Straight, ribbed and multi. crack
	49.03	92.52	10.65	3.46	0.131	100	Straight, ribbed and multi. crack
	98.07	129.88	10.78	3.08	0.423	100	Straight, ribbed and bridged
$B6_I$	1.96	16.76	13.13	3.19	0.268	27	Improper cracks and chipping
	2.94	21.01	12.47	3.05	0.552	80	Multiple cracks
	4.90	27.01	12.48	3.07	0.378	63	Multiple cracks
	9.81	39.27	11.82	3.51	0.288	50	Multiple cracks
$B7_I$	1.96	16.61	13.24	2.85	0.293	45	Improper cracks and chipping
	2.94	21.80	11.61	3.19	0.514	75	All types
	4.90	29.12	10.87	2.60	0.184	69	All types
	9.81	39.91	11.46	3.25	0.193	67	Straight and multiple cracks
	24.52	62.97	11.49	3.30	0.320	89	Straight and multiple cracks
	49.03	92.58	10.62	3.23	0.253	100	Bridged and strat., ribbed crack
	98.07	133.25	10.24	3.13	0.349	67	Bridged and strat., multi. cracks
	SENB			3.35	0.710		
$C1_I$	2.94	22.72	10.89	2.51	0.191	78	Bowing
	4.90	29.97	10.24	2.27	0.394	100	Bridged and bowing
	9.81	42.93	9.89	2.99	0.326	86	Bowing and straight cracks
	24.52	70.49	9.22	2.78	0.273	88	Bowing and straight cracks
	49.03	98.54	9.41	3.06	0.362	100	Bridged with extra cracks
	98.07	135.48	9.92	3.37	–	100	Bridged with extra cracks
$C2_S$	1.96	18.17	10.88	–	–	0	Not identifiable in two corners
	2.94	21.38	10.60	2.75	0.362	67	Fairly straight and bowing
	4.90	30.40	10.00	3.10	0.318	63	Fairly straight and bowing
	9.81	43.56	9.62	3.40	0.391	50	Fairly straight and bowing
	24.52	68.50	9.71	3.38	0.336	60	Multicracked, bridged and straight
	49.03	98.62	9.35	3.52	0.124	60	Multicracked, bridged and straight
$C2_S$iv	1.96	17.89	11.43	2.95	0.456	33	All types
	2.94	23.04	10.39	2.68	0.297	66	Zigzag
	4.90	29.13	10.74	2.54	0.209	90	Zigzag and branched
	9.81	43.51	9.62	3.06	0.087	50	Zigzag and multiple cracks
$C2_S$vi	1.96	18.16	11.10	–	–	0	Improper crack formation
	2.94	22.99	10.44	1.69	0.219	63	Multiple cracks
	4.90	30.45	9.97	3.21	0.682	33	Multiple cracks
	9.81	46.00	8.61	2.83	0.093	90	Multiple crack and branched
	SENB			2.91	0.185		
C5	1.96	18.54	10.69	–	–	0	Not identifiable in two corners
	2.94	23.32	10.13	2.68	0.259	50	Not identifiable in all corners
	4.90	29.34	10.60	2.83	0.469	88	Fairly straight and bowing
	9.81	42.86	9.92	3.13	0.330	91	Fairly straight and bowing
	24.52	70.01	9.30	3.10	0.241	67	Multiple crack and branched

(*continued on next page*)

Table 2 (*continued*)

Material code	Load (N)	d (μm)	Hv (GPa)	K_{ic} (MPa $m^{1/2}$)	Std. dev. of K_{ic}	% OK crack system	Nature of cracks
	49.03 SENB	97.53	9.58	3.58 3-4[a]	0.310	90	Multiple crack and branched
$D2_S$	1.96	–	–	–	–	0	Not identifiable in all corners
	2.94	22.48	10.85	3.62	–	25	Not identifiable in two corners
	4.90	33.28	8.34	2.14	0.227	63	Straight crack
	9.81	44.58	9.19	2.13	0.326	57	Bowing
	24.52	70.28	9.24	1.85	0.307	31	Bridged and multiple crack
	49.03	104.63	8.39	3.29	0.534	40	All types
$A7_R$	2.94	21.84	11.48	3.23	0.525	44	Bow/straight and extra cracks
	4.90	27.70	11.87	3.36	0.238	60	Bowing and extra cracks
	9.81	39.17	11.88	3.64	0.445	80	Fairly straight
	24.52	61.87	11.88	3.52	–	100	Bowing and extra cracks
	49.03	86.80	12.07	3.78	0.408	100	Strat., bowing and multiple crack
$A8_R$	1.96	18.13	11.07	–	–	0	Not identifiable in all corners
	2.94	21.96	11.33	2.76	0.301	67	Bowing, zigzag and extra crack
	4.90	28.35	11.36	3.32	0.380	85	Bowing and extra cracks
	9.81	40.83	10.93	3.19	0.396	75	Bowing and extra cracks
$C7_{A16}$	2.94	20.84	11.59	2.71	0.406	100	Fairly straight and bowing
	4.90	29.65	10.44	2.27	0.478	70	Fairly straight and bowing
	9.81	42.21	10.25	3.00	0.603	85	Fairly straight and bowing
	24.51	65.98	10.48	3.40	0.385	100	Fairly straight and bowing
	49.03	93.03	10.53	2.84	0.333	100	Bridged or straight with rib
	98.07	131.04	10.60	3.02	0.469	86	Bridged or straight with rib
$H6_S$	1.96	18.46	10.79	1.91	0.461	45	Improper cracks and chipping
	2.94	22.78	10.65	2.04	0.469	82	Zigzag, extra cracks and bowing
	4.90	28.25	11.40	2.88	0.307	60	Multiple cracks
	9.81	37.40	11.55	3.31	0.659	50	Multiple cracks
	24.52	64.79	10.86	3.38	0.691	100	Multiple crack and bridged
	49.03	91.95	10.77	3.31	0.756	100	Multiple crack and bridged
$H3_S$	1.96	16.40	13.59	2.76	–	44	Fairly straight and bowing
	2.94	20.72	12.90	2.73	–	29	No crack, only two readings
	4.90	27.45	12.13	2.94	0.235	64	Fairly straight and bowing
	9.81	37.68	12.82	3.17	0.446	90	Fairly straight
	24.52	61.55	12.02	3.06	0.415	80	Straight and multiple crack
	49.03	85.46	12.45	2.61	0.180	100	Straight and multiple crack
$H3_{A16}$	2.94	19.70	14.06	3.27	0.339	60	Not identifiable in all corners
	4.90	25.83	13.65	4.20	0.296	100	Fairly straight and bowing
	9.81	38.82	12.12	3.48	0.587	100	Fairly straight and bowing
	24.52	60.93	12.26	3.11	0.320	100	Fairly strat., zigzag and bowing
	49.03	89.82	11.33	3.99	0.342	100	Fairly strat., zigzag and bowing

The plot of 'Knoop hardness against load' for various LPS materials is seen in Fig. 3. A higher hardness observed at lower load in the said figure, well known as "indentation-size effect", is found to be pronounced in the materials containing a higher SiO_2 in the chemical composition. Further, it is interesting to note that such an effect on Vickers hardness (H_v) is relatively low (Table 2).

3.3. *Effect of microstructure on* H_o *and* E

Fig. 4(a) shows a strong dependence ($r^2 = 0.81$) of E on sintered density for 89–94% LPS materials. Whereas a relatively weak relationship ($r^2 = 0.68$) between H_o and sintered density has been observed as seen in the Fig. 4(b). Therefore, H_o and E are mutually interrelated ($r^2 = 0.48$) here due to their density dependent property. In our previous study, it has been shown that the increase in SiO_2 content results in a lower sintered density [18]. With the increase in SiO_2 content, a declining trend in H_o is observed (Fig. 5) for all the three varieties of powders. Fig. 6 shows the effect of $MgO/(CaO + BaO + KNaO)$ on H_o for the selected LPS materials derived from coarse, medium and reactive powders with SiO_2 content in the range 4.3–5.2 wt%. As is seen, the coarse variety shows a steep decline, whereas the medium and the reactive varieties show a marginally upward trend in the corresponding H_o.

In general, H_o for the LPS materials derived from reactive Al_2O_3 powders has been found to be higher than that of the coarse and medium powders (Figs. 5 and 6). For instance, $A8_R$ has a higher hardness (Table 3) than $A1_I$ while the chemical compositions are nearly the same. The substantial rise in hardness can not, however, be attributed

Table 3
Mechanical properties of LPS Al_2O_3 ceramics with different commercial powders

Material code	Maximum size of:		H_o (GPa)	E		Flexural strength	
	grains (μm)	voids (μm)		$\bar{X}$ (GPa)	σ	$\bar{X}$ (MPa)	σ
$A1_I$	27.8	204.0	8.82	270	0.8	343	31.1
$A2_M$	43.4	61.3	10.67	290	1.4	260	18.2
$A5_o$	29.8	55.0	9.70	280	1.7	–	
$A6_M$	41.5	95.8	10.47	310	2.1	255	28.8
$B1_S$	28.0	61.0	9.62	300	1.2	186	23.4
$B6_I$	27.9	60.6	12.14	303	0.7	230	33.2
$B7_I$	25.8	106.3	9.92	280	1.1	349	29.1
$C1_I$	20.0	30.0	9.77	272	0.4	–	
$C2_S$	36.9	55.6	8.53	272	1.8	187	36.4
$C5_o$	12.0	107.0	9.07	276[a]		330[a]	
$C2_S$iv	35.0	150.0	8.22	266	3.7	189	
$A7_R$	18.5	44.9	12.34	315	0.6	288	55.5
$A8_R$	33.1	31.4	11.14	288	10.7	–	
$C6_R$	32.9	125.0	–	269	1.0	285	39.9
$C7_{A16}$	9.0	40.9	11.55	264	2.1	–	
$D2_S$	35.0	61.0	7.91	251	1.3	301	21.0
$H6_S$	17.8	41.3	10.38	305	13.9	–	
$H3_{A16}$	45.3	45.7	11.57	332	0.6	337	34.3
$H3_R$	44.2	55.1	13.60	303	0.9	232	33.1

[a] Published data.

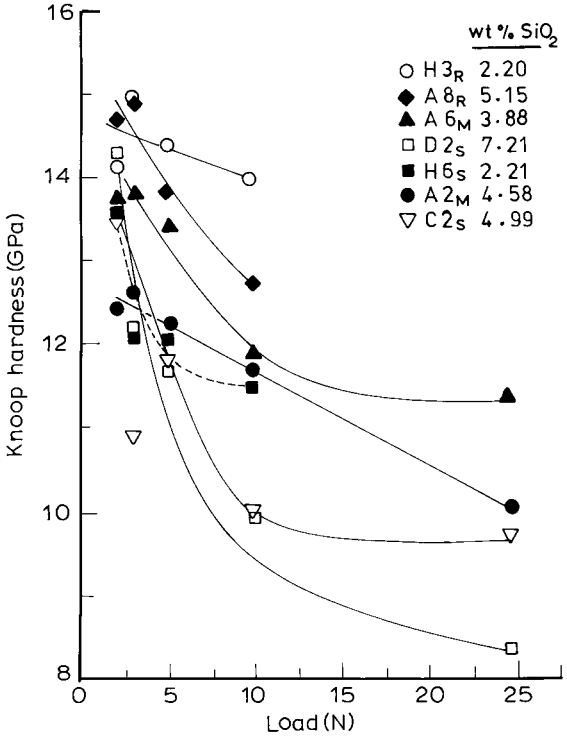

Fig. 3. Knoop hardness versus applied load for different LPS Al_2O_3 ceramics showing the influence of SiO_2 content.

to the grain size of the sintered material either because the average grain size (Feret dia) in both the materials are similar (see Table 1 for $A8_R$ and Fig. 1 for $A1_I$). The reason for such an increase in the hardness can be explained from the differences in the Al_2O_3 content of the intergranular glassy phase occurring during sintering. The alkaline earth silicates are known [23] to form a reactive liquid phase that dissolves Al_2O_3 during sintering. Upon cooling, the liquid phase transforms into the glassy phase with or without partial crystallization of certain phases. The extent of crystallization, however, depends on the composition and kinetics of cooling. When Al_2O_3 rich liquids solidify, the dissolved Al_2O_3 is forced to enter into the glass-structure in the form of AlO_4-network. The presence of AlO_4-network in a similar composition has been shown by a FTIR spectroscopy [24]. The reactive powders are easily dissolved into the liquid phase during the sintering process and a higher amount of Al_2O_3 is, thus, retained in the glassy state. In the present LPS materials derived from the reactive powders, both the EDS analyses and the experimental data on solubility tests of different Al_2O_3 powders in glass [20] have shown a relatively higher amount of Al_2O_3 in the intergranular glassy phase. Hardness of Al_2O_3 rich glass is higher [19] that leads the hardness of the present Al_2O_3–glass composite high.

The dependence of the mechanical parameters such as E, H_o, flexural strength and $K_{ic\text{-}short}$ at different indentation load for 89–94% LPS Al_2O_3 on $G^{-1/2}$ has been examined by regression analyses. A wide scatter has been observed with no definite trend or any significant relationship. A maximum value of r^2 (=0.21) is obtained in the case of $G^{-1/2}$ versus H_o. The relationship between aspect ratio and the said mechanical parameters also did not indicate any significant relationship.

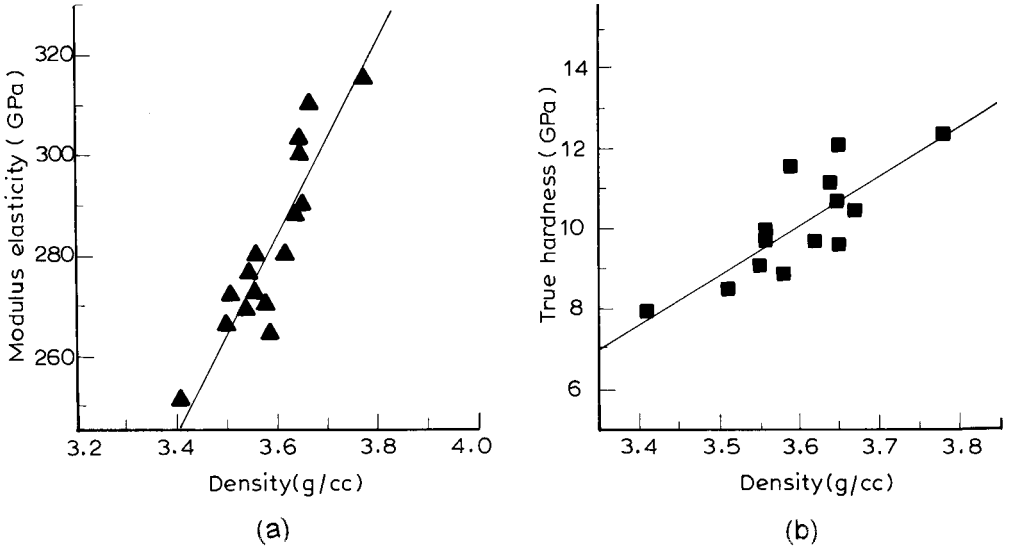

Fig. 4. Effect of density on (a) modulus of elasticity, (b) true hardness of different 89–94% wt% LPS Al_2O_3 ceramics.

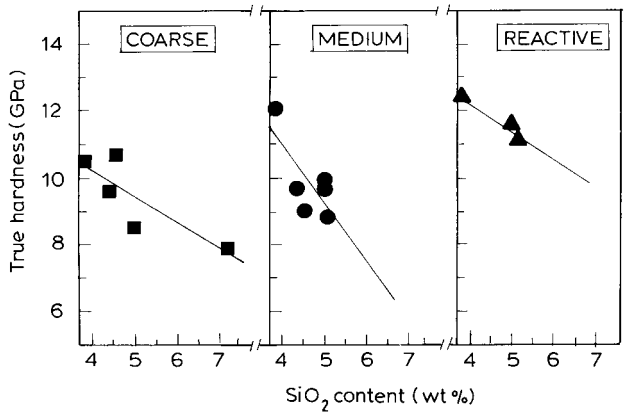

Fig. 5. Role of SiO_2 content on true hardness of 89–94% LPS Al_2O_3 ceramics derived from different powders.

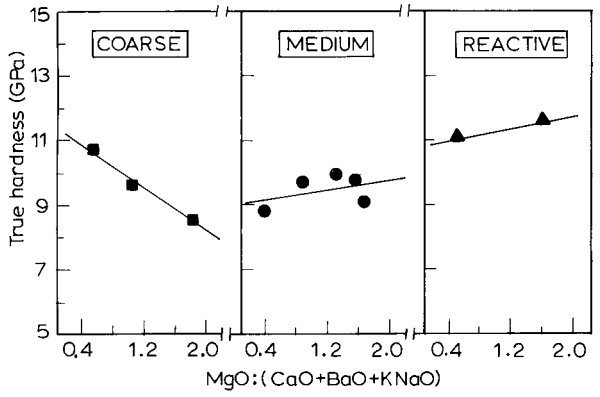

Fig. 6. Effect of MgO/(CaO + BaO + KNaO) ratio on true hardness of selected 91–94 wt% LPS Al_2O_3 with SiO_2 content in the range of 4.3–5.2 wt%.

3.4. Effect of indentation load and microstructure on fracture path

When the speed of the indentor remains constant, the rate of loading/unloading changes with the applied load. In a fine grained polycrystalline Al_2O_3, Salomonson et al. [25] observed that the fracture from the slow unloading is predominantly intergranular whereas that of the fast unloading is transgranular. Bhargava et al. [26] reported a similar observation for different ceramic composites. Thus, the intergranular fracture is expected during the low load regime (1.96–2.94 N). SEM images of the indentation crack, however, show the presence of transgranular cracks in both the $A1_I$ [Fig. 7(a)] as well as $C1_I$ [Fig. 7(b)] materials.

At higher indentation load in between 4.90 and 49.03 N, the fracture mode is observed to be different. As seen in Figs.7(c) and 8(a), a predominantly intergranular fracture is observed in $A1_I$. On the other hand, a relatively higher proportion of transgranular fracture is seen in $C1_I$ [Fig. 7(d)]. The change in the fracture mode can be explained from the interfacial thermal expansion mismatch stresses arising out of the compositional differences. The thermal expansion coefficient of the intergranular glassy phase can be estimated from that of the reported glass compositions. The thermal expansion [19] of high-CaO glass ($\alpha = 9.5\times10^{-6}/°C$) is much higher than high-MgO glass ($\alpha = 5.0\times10^{-6}/°C$) and is also higher than Al_2O_3 in some crystallographic direction ($\alpha_a = 8.6\times10^{-6}/°C$). When the thermal expansion coefficient of the grain boundary phase is greater than that of the Al_2O_3, both the tensile stress in the grain boundary and the compressive stress in the Al_2O_3 grain should increase as the thermal expansion coefficient of the grain boundary phase increases. Thus the interface between Al_2O_3 and the high-CaO glass will experience tensile stress resulting in a weaker boundary. The glass modifiers in the composition, e.g. BaO, Na_2O and K_2O influenced

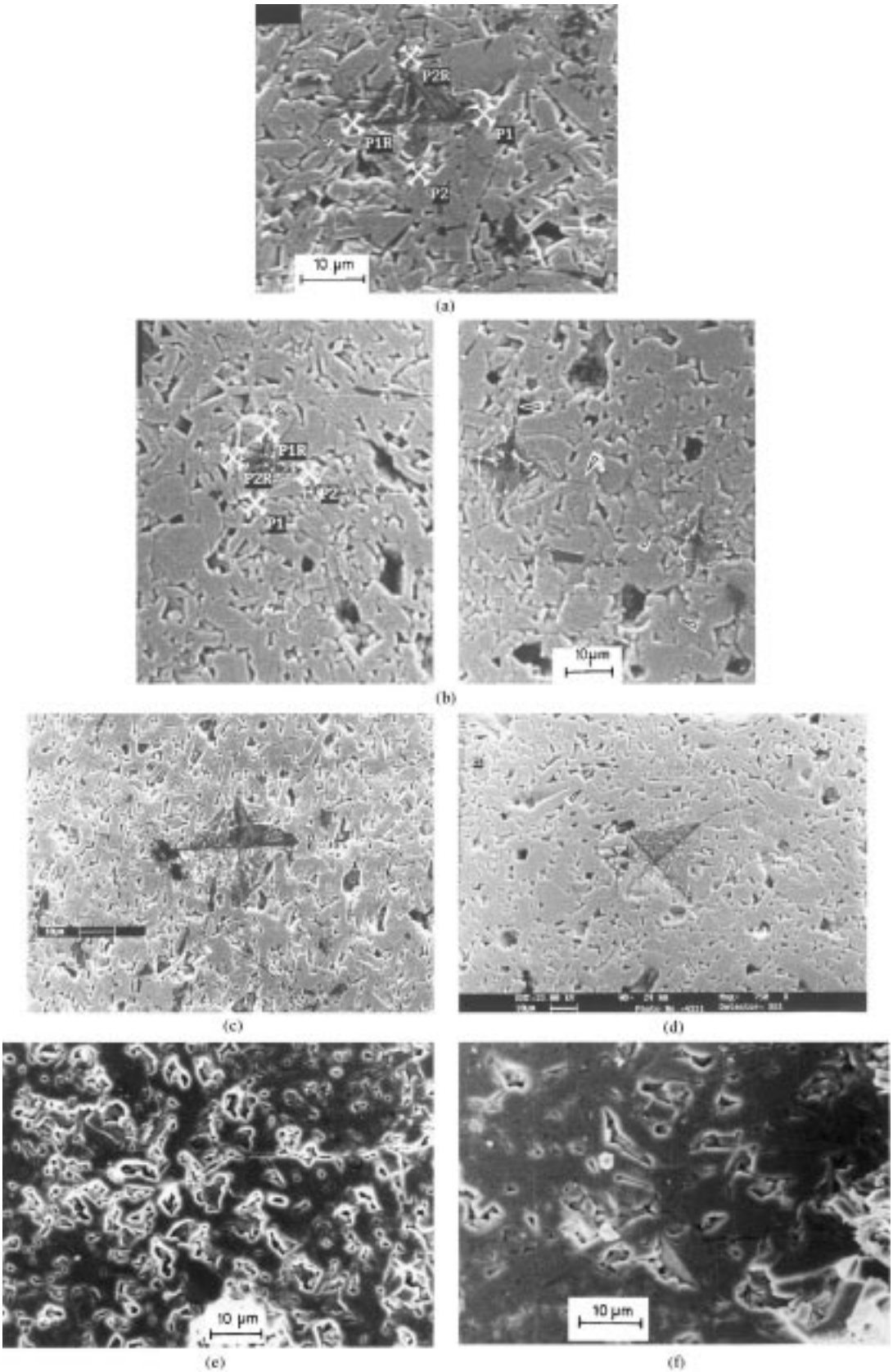

Fig. 7. Indentation cracks of 91–94 wt% LPS Al_2O_3 ceramics: (a) $A1_I$ at 2.94 N; (b) $C1_I$ at 1.96 and 2.94 N; (c) $A1_I$ at 4.90 N; (d) $C1_I$ at 9.81 N; (e) $B1_S$ at 98.07 N; (f) $A6_M$ at 49.03 N load. Arrows indicate the transgranular fractures. Note the smaller sizes of the bridging grains in $B1_S$.

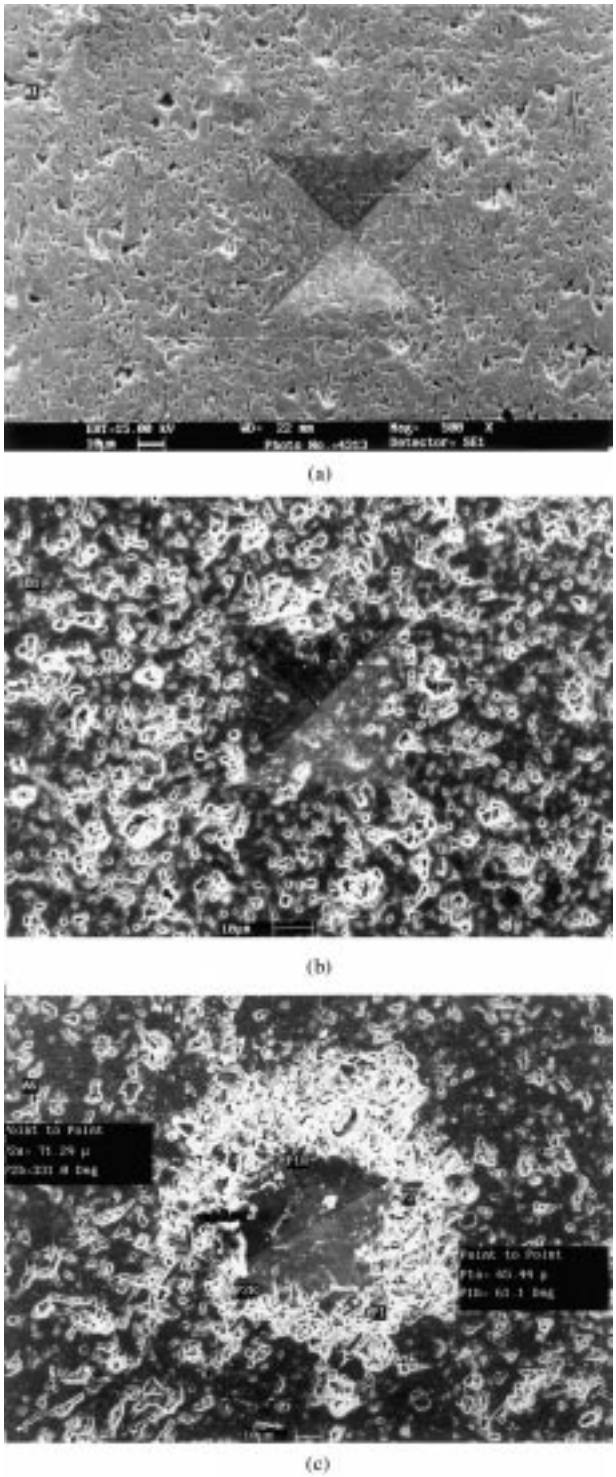

Fig. 8. SEM images of the indentations (24.52 N load) for (a) $A1_I$, (b) $B1_S$, and (c) A6 $_M$ showing local microfracture in A6 $_M$ and intergranular crack in $A1_I$.

the thermal expansion in a similar manner [19] as that of the CaO. Hence, the thermal expansion mismatch stresses is tensile in the grain boundary region of $A1_I$ due to a low MgO/(CaO + BaO + KNaO) ratio. The intensity of this tensile stress is in decreasing order through the series of the compositions beginning from $A1_I$ to $B7_I$ and with further increase in the ratio to ~1.6 as in C-type, a compressive stress field is expected in the grain boundary glass. The crack is deflected towards the Al_2O_3 grains [Fig. 7(d)] due to compressive stress field in the grain boundary glass.

The higher crack length of $A1_I$ (Fig. 2) at lower indentation load can also be explained from the internal tensile stresses arising out of thermal expansion mismatch between Al_2O_3 and high CaO-glass. The weak grain boundary due to the residual tensile stresses has also been responsible for crack branching that is observed in $A1_I/A2_M$ materials (Table 2). At higher indentation load (49.03 N), however, the crack length is nearly the same as that of the $B1_S$ (Fig. 2) due to the activation of crack arresting mechanisms like deflection and bridging from the large elongated grains upon crack extension [Fig. 8(a)]. Although the grain size distribution and morphology in $B1_S$ and $C1_I$ are similar [27], the crack length in $C1_I$ is much higher as seen in Fig. 2, probably due to joining of radial cracks [28].

The fracture modes in $B1_S$ [Fig. 7(e)] and $A6_M$ [Fig. 7(f)] are also intergranular, but there is a distinct difference in their fracture behavior. In $B1_S$, a nearly perfect indentation crack system is observed with single crack originating from the corners of the Vickers indentation — symmetric, fairly straight and occasionally with bowing as seen in Fig. 8(b). Whereas the indentation in $A6_M/B6_I$ is associated with the local microfracture [Fig. 8(c)] and multiple cracks originated from the corners/sides. Optical microscopic images in Fig. 9 show a typical zigzag/multiple crack system in $A6_M$ and the straight/bowing crack system in $B1_S$. Observations on the crack systems formed at different load have been mentioned in Table 2 with the percentage of successful readings. $B1_S$ shows a relatively higher percentage of successful readings than $A6_M$. Although the average grain sizes in these two materials are nearly the same [18], but the grain size distribution in the microstructure is widely different. As can be seen in Fig. 10 that $A6_M$ has a higher proportion of large-sized (> 12 μm) grains distributed in a fine-grained (~2 μm) matrix. The micrographs in Fig. 11 show that the grains are equiaxed in $B1_S$ and elongated in $A6_M$. The low stress-intensity at the boundaries of equiaxed grains is probably responsible for the lower crack length in $B1_S$. Although the crack deflection [14,15,29] from the elongated grain is seen extensively [Fig. 7(f)] in $A6_M$, the crack length is similar to $B1_S$.

EDS analyses carried out in two different materials have shown that the chemical compositions vary between the poles and sides of the elongated grains. Table 4 shows the differences in MgO/(CaO + BaO + KNaO) ratio calculated from the EDS analyses. A low ratio at the sides would result in a residual tensile stress and a high ratio at the poles in a compressive stress. The crack is expected to travel through the weak interface [30], i.e.

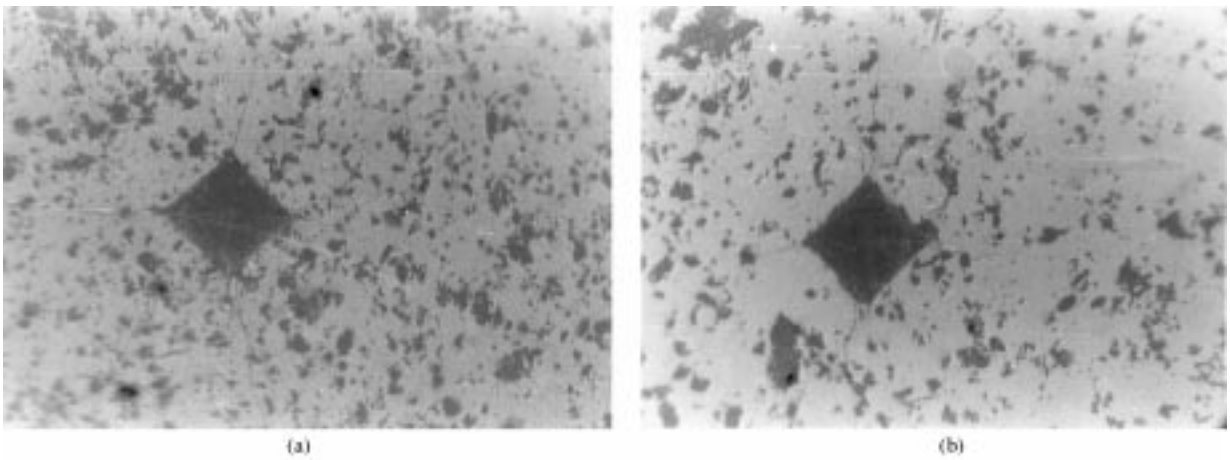

Fig. 9. Optical micrographs showing indentation cracks of (a) fairly straight/bowing nature in $B1_S$ and (b) multiple/zig-zag nature in $A6_M$ at 49.03 N of load.

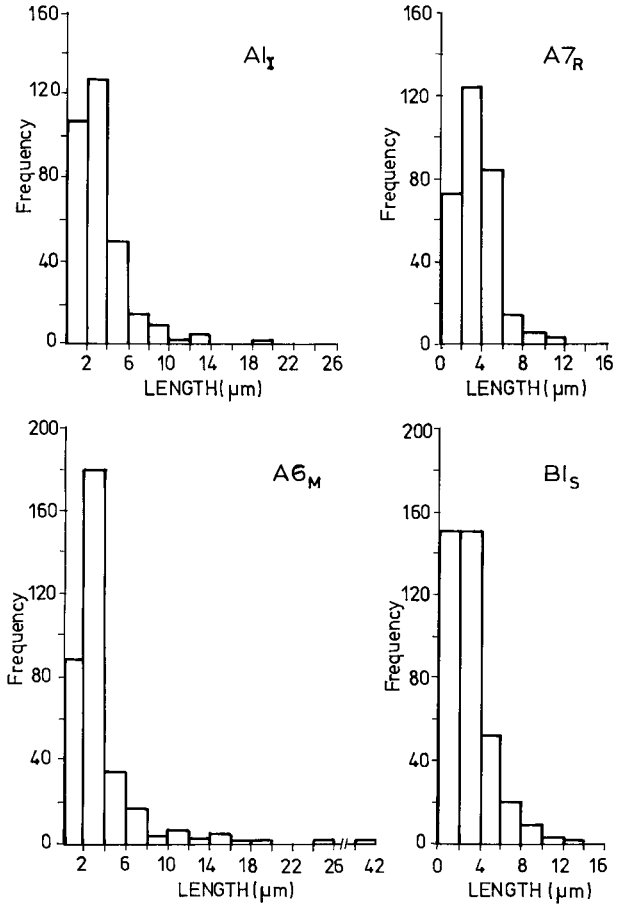

Fig. 10. Grain size (major axis) distribution of certain selected LPS Al_2O_3 ceramics derived from different powders.

along the sides of the large elongated grains, which is seen in Figs. 7(f) and 8(a). Crack deflection and bridging in LPS Al_2O_3 is therefore associated with the thermal expansion mismatch stresses due to compositional differences within the microstructure.

3.5. *Effect of microstructure on* $K_{ic\text{-}short}$

The general trend of $K_{ic\text{-}short}$ in 89–94% LPS material is that it is higher at 1.96–2.94 N load, lower at 4.90 N and then rising with an increasing load upto 49.03 N beyond which no further rise has been observed (Table 2). A higher $K_{ic\text{-}short}$ is observed in both the $A6_M$ and $B1_S$ materials where the MgO/(CaO + BaO + KNaO) ratio is ~1.0. The higher $K_{ic\text{-}short}$ in $A1_I$ at the higher indentation load (49.03 N) can be attributed to the presence of higher-sized (Fig. 10) elongated grains — an observation consistent with the study on self-reinforced silicon nitride [31].

A higher $K_{ic\text{-}short}$ is also observed (Table 2) in the $A7_R$ material derived from the reactive powder where the MgO/(CaO + BaO + KNaO) ratio is as low as 0.19%. As explained earlier, the dissolution of Al_2O_3 in the grain boundary glass is higher with the reactive powder. The thermal expansion of high CaO-glass is substantially reduced when the glass is rich in Al_2O_3 [19]. Therefore, the $K_{ic\text{-}short}$ at lower load is significantly higher compared to $A1_I$. It is to be noted that the grains in $A7_R$ have equiaxed morphology, narrow size distribution [Fig. 1(c), Table 1] and free from reinforcement grains for activating the microstructural shielding (Fig. 10). It means that a reduced tensile thermal expansion mismatch stresses can result in a higher fracture resistance at the lower applied load regime.

The $K_{ic\text{-}short}$ in $C7_{A16}$ is low as in $C1_I$. When the grain size is increased, $K_{ic\text{-}short}$ increases at higher loads while at lower loads it remains unchanged as seen in Fig. 12. Similar effect is also seen in the case of $H3_R$ and $H3_{A16}$ where an increase in grain size (Table 1) is found to enhance the $K_{ic\text{-}short}$. Residual thermal expansion stresses associated with increased grain size is responsible for the rising $K_{ic\text{-}short}$ with increased grain size. The difference in $K_{ic\text{-}short}$ between $C1_I$ and $C5_o$ in Fig. 12 can probably be explained from the higher glass

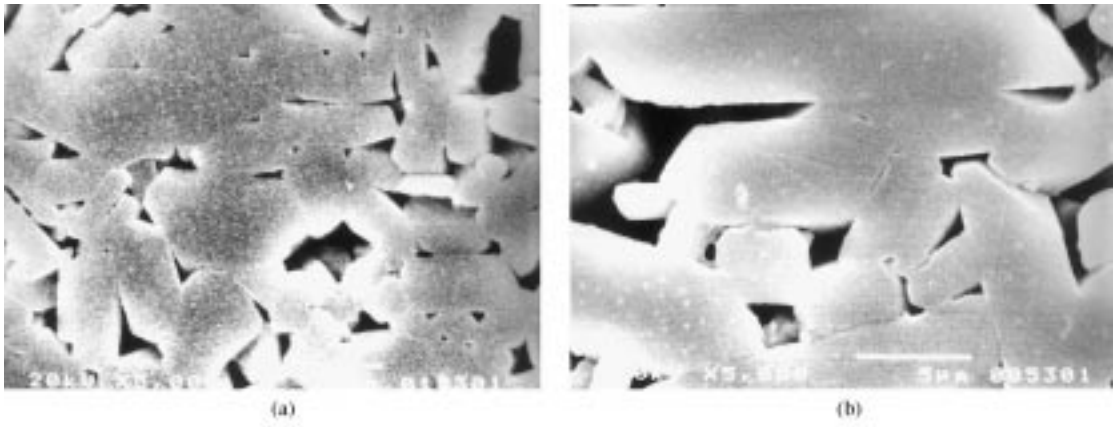

Fig. 11. SEM micrographs of (a) $B1_I$ and (b) $A6_M$ showing the differences in size and morphology of Al_2O_3 grains.

Table 4
MgO/(CaO + BaO + KNaO) ratio at different locations of elongated grains in LPS Al_2O_3

Location	$A2_M$	$H3_{A16}$
Along the elongated axis	0.45	0.40
End of the elongated axis	1.75	1.72

transition temperature [19] due to lower SiO_2 content in $C5_o$.

Although the $K_{ic\text{-}short}$ of $B6_I$ is lower than $A6_M$, the crack length is nearly the same [32]. The higher E/H_o value (Table 3) is responsible for the increased $K_{ic\text{-}short}$ in $A6_M$. Similar argument can account for the improvement in the toughness of $H3_{A16}$ over $H3_S$. Further, the grain size distribution of $H3_{A16}$ [Fig. 1(d), Table 1] is similar [27] to $A6_M$. The toughening from the reinforcement grains is realized in this material in addition to the contribution from higher E/H_o value. The observation is pertinent to the wear applications [27] where the material removal process is by damage accumulation and grain dislodgment. The materials $A2_M$, $A5_o$, $H6_S$ and $D2_S$ show lower $K_{ic\text{-}short}$ due to a higher and broad grain size distribution in the microstructure [33].

Among the various intergranular crystalline phases, the anorthite phase has a thermal expansion ($\alpha = 11.0\times10^{-6}/°C$) higher than that of the Al_2O_3. Therefore, the precipitation of anorthite phase is likely to influence the $K_{ic\text{-}short}$ in a similar manner as that of the low MgO/(CaO + BaO + KNaO) ratio in the glass composition. A substantial amount of anorthite phase is present in both the 'A' and 'B' type materials, whereas it is negligible [20] (by X-ray detection) in 'C' type materials. With a view to evaluate the effect of anorthite precipitation in the grain boundary, the $C2_S$ material has been separately heat treated for 2 h at 1400°C maintaining a similar cooling schedule as that of the sintering. Both the hardness and $K_{ic\text{-}short}$ in this material

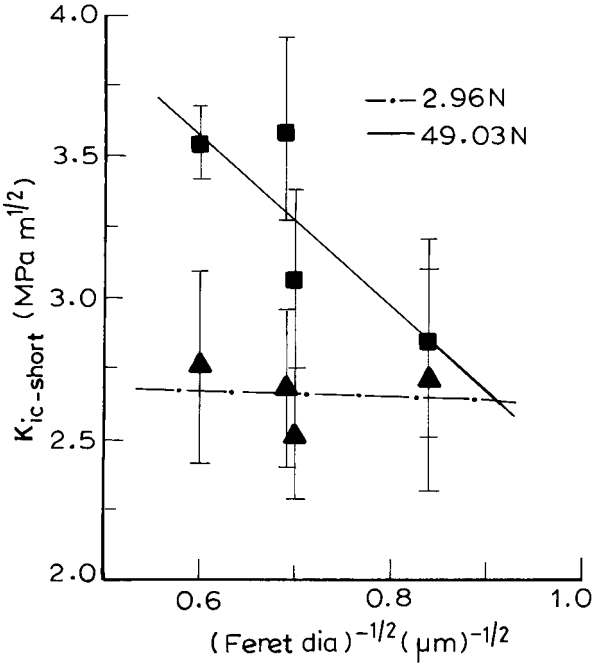

Fig. 12. Grain size dependence of $K_{ic\text{-}short}$ at the 2.96 N and 49.03 N load in 91–94 wt% Al_2O_3 LPS ceramics with MgO/(CaO + BaO + KNaO) ratio ~1.6.

($C2_S$iv) have been found to be lower as seen in the Tables 2 and 3. The residual thermal expansion mismatch stresses generated due to anorthite phase in 'C' type materials is different than in 'A' type. TEM investigations in LPS materials have shown that the precipitation of anorthite occurs on Al_2O_3-surface and not within the grain boundary glass [16,20]. Thus, the 'Al_2O_3-(MgO) glass' interface of $C2_S$ may have changed to 'Al_2O_3–anorthite–(MgO) glass' interface in $C2_S$iv. Accordingly the thermal expansion mismatch stresses changed from compressive to tensile resulting in a low $K_{ic\text{-}short}$. Interestingly, the crack path has been observed to be similar in nature with the 'A' type (Table 2). Although the composition of $B7_I$ is close to the 'C' type, the crack path featured similarities with $C2_S$iv or

'A' type. This is because of anorthite precipitation in $B7_I$ is of similar magnitude as that of the $C2_S$iv. The decrease of H_o in $C2_S$iv can be explained from the lower hardness of the glass depleted in CaO [19].

Thus, the interfacial thermal expansion mismatch stresses at the grain boundary region arising out of the (1) composition of intergranular glassy phase, (2) precipitation of anorthite phase and (3) average grain size, influence the $K_{ic\text{-}short}$ at the low load regime whereas the aspect ratio, shape and size of reinforcement grains determines the $K_{ic\text{-}short}$ at high load regime.

3.6. Flexural strength and fracture toughness

Table 3 shows that a high flexural strength has resulted with (1) medium powder (I-grade) in the case of the 91–94 wt% Al_2O_3, (2) coarse powder (S-grade) in the case of 88–90 wt% and (3) reactive powder (A16SG-grade) in the case of 95–97 wt% LPS materials. Considering all the varieties, $B7_I$ has the highest flexural strength where the $K_{ic\text{-}long}$ is also higher. Fractographic analysis shows that the failure has occurred either from the defects like a large grain or a void or a foreign particle. As is known that failure usually occurs from a flaw of critical size and once the flaw is sufficiently large, the crack propagates in catastrophic manner. Table 3 shows that no relationship can be made with the maximum grain size or void size in the microstructure. The void size would have been enlarged during the operations like cutting, grinding and polishing employed for the preparation of the specimen. It is interesting that the cleavage fractures noticed in the large elongated grains did not affect the flexural strength.

4. Conclusions

Starting powder characteristics and chemical composition were found to influence the mechanical properties of LPS Al_2O_3 ceramics due to the differences in the microstructure. A higher amount of Al_2O_3 dissolved into the grain boundary glassy phase in the case of reactive powders resulted in higher hardness and indentation fracture toughness. LPS derived from a powder of 3–7 μm in size resulted in a maximum flexural strength. A decrease in SiO_2 content in LPS composition produced higher modulus of elasticity and hardness. MgO/(CaO + BaO + KNaO) ratio of nearly 1 in the LPS resulted in a high $K_{ic\text{-}short}$ for coarse powders.

The mode of fracture changed not only with the indentation load but also with the MgO/(CaO + BaO + KNaO) ratio in the LPS. Fractures resulting either from a low indentation load (1.94–4.90 N) or a slow loading/unloading rate had relatively higher proportion of transgranular cracks. At the higher load (> 9.81 N), cracks were intergranular when the MgO/(CaO + BaO + KNaO) ratio was nearly 1.0 and transgranular when the ratio was nearly 1.6. A higher grain size in the latter showed an improved $K_{ic\text{-}short}$ at higher indentation load (49.03 N) and upon precipitation of anorthite phase in the same material resulted a lower $K_{ic\text{-}short}$. The thermal expansion coefficient of the grain boundary phases either similar but not higher than Al_2O_3 associated with a higher E/H_O and a fine-grained microstructure with reinforcement grains resulted in a higher $K_{ic\text{-}short}$.

The crack path was bowing at the lower indentation loads (< 9.81 N). At higher indentation loads (⩾24.52 N), the crack path was influenced by the grain size distribution in the microstructure. A fine-grained (major axis < 12 μm) microstructure showed a fairly straight crack and the one with coarse grains (major axis > 12 μm) showed a zigzag crack. Crack branching was observed in the LPS materials of low MgO/(CaO + BaO + KNaO) ratio. A coarse-grained microstructure (Feret dia > 3.0 μm) with a broad grain size distribution produced multiple cracks and such a microstructure resulted in a low indentation fracture toughness.

Acknowledgements

Authors thank BHEL management for the necessary support. The observations made by Mr. L.K. Sachdeva, former National Project Director of CTI is gratefully acknowledged. Thanks to Professor Brian Lawn, NIST, USA and Professor Vikram Jayaram, IISc, India for valuable suggestions.

References

[1] R.W. Rice, Microstructure dependence of mechanical behavior of ceramics, in: R.C. McCrane (Ed.), Treatise on Materials Science and Technology, vol. II, Academic Press, New York, 1977, pp. 199–381.
[2] T.F. Page, G.R. Sawer, O.O. Adewoye, J.J. Wert, Hardness and wear behavior of SiC and Si_3N_4 ceramics, Proc. Br. Ceram. Soc. 26 (1978) 193–208.
[3] G.R. Antis, P. Chantikul, B.R. Lawn, D.B. Marshall, A critical evaluation of indentation techniques for measurement of fracture toughness: I. Direct crack measurements, J. Am. Ceram. Soc. 64 (9) (1981) 533–538.
[4] D.B. Marshall, B.R. Lawn, R.F. Cook, Microstructural effect on grinding of alumina and glass-cramics, J. Am. Ceram. Soc. 70 (1987) C139–140.
[5] R.W. Rice, C.C. Wu, F. Borchett, Hardness-grain size relations in ceramics, J. Am. Ceram. Soc. 77 (10) (1994) 2539–2553.
[6] D.J. Clinton, R. Morell, Hardness of Al_2O_3 Ceramics, Proc. Br. Ceram. Soc. 34 (1984) 113–127.
[7] L.M. Braun, S.J. Bennison, B.R. Lawn, Objective evaluation of short-crack J toughness curves using indentation flaws: case study on alumina based ceramics, J. Am. Ceram. Soc. 75 (11) (1992) 3049–3057.
[8] A. Linan, H.M. Chan, *R*-curve behavior of in-situ toughened Al_2O_3–$CaAl_{12}O_{19}$ ceramic composites, J. Am. Ceram. Soc. 79 (12) (1996) 3142–3148.

[9] R.F. Cook, Segregation effects in the fracture of brittle materials: Ca–Al_2O_3, Acta Metall. 38 (6) (1990) 1083–1100.
[10] N.P. Padture, H.M. Chan, Improved flaw tolerance in alumina containing 1 vol% anorthite via crystallization of the intergrannular glass, J. Am. Ceram. Soc. 75 (7) (1992) 1870–1875.
[11] N.P. Padture, S.J. Bennison, H.M. Chan, Flaw tolerances and crack-resistance properties of alumina–aluminium titanate composites with tailored microstructures, J. Am. Ceram. Soc. 76 (9) (1993) 2312–2320.
[12] F.F. Lange, Interaction of a crack front with a second phase dispersion, Philos. Mag. 22 (179) (1970) 983–992.
[13 R.F. Cook, B.R. Lawn, C.I. Fairbanks, Microstructure strength properties in ceramics: I. Effect of crack size on toughness, J. Am. Ceram. Soc. 11 (1985) 604–615.
[14] P.F. Becher, Microstructure design of toughened ceramics, J. Am. Ceram. Soc. 74 (2) (1991) 255–269.
[15] W.A. Zdaniewski, H.P. Kirchener, Toughening of a sintered alumina by crystallization of the grain-boundary phase, Adv. Ceram. Mater. 1 (1986) 99–103.
[16] C.A. Powell-Dogan, A.H. Heuer, Microstructure of 96% alumina ceramic: III Crystallization of high calcia boundary glasses, J. Am. Ceram. Soc. 73 (12) (1990) 3684–3691.
[17] N.P. Padture, H.M. Chan, influence of grain size and degree of crystallization of intergrannular glassy phase on mechanical behaviour of a debased alumina, J. Mater. Sci. 29 (1991) 2711–2715.
[18] A.P. Goswami, S. Roy, G.C. Das, M. Mitra, Impurity dependent morphology and grain growth in LPS alumina. J. Am. Ceram. Soc., submitted for publication.
[19] N. Bansal, R.H. Doremus, Handbook of Glass Properties, Academic Press, Orlando, 1986, pp.145–170 & 335–349.
[20] A.P. Goswami, S. Roy, G.C. Das, M. Mitra, Influence of powder, chemistry and microstructure on the wear resistance of liquid-phase-sintered Al_2O_3 Wear, submitted for publication.
[21] R.C. Bradt, et al. (Eds.), Fracture Mechanics of Ceramics, Vol. 10, Plenum Press, New York, 1992. pp. 119–133.
[22] Designation C848-88 ASTM, 1916 Race St., Philadelphia, PA, USA.
[23] W.D. Kingery, H.K. Bowen, D.R. Uhlmann, Introduction to Ceramics, 2nd ed. John Wiley and Sons, New York, 1976. pp. 498–501.
[24] S. Venkataraman, Alumina–glass ceramics composites, Bull. Mater. Sci. 18 (7) (1995) 845–856.
[25] J. Salomonson, D.J. Rowcliffe. Presented at the 98th Annual Meeting of the American Ceramic Society, Indianapolis, IN, 1996 (Paper No. BP-3–96).
[26] P. Bhargava, B.R. Patterson, Quantitative characterisation of indentation crack path in cubic zirconia–10 vol% alumina composite, J. Am. Ceram. Soc. 80 (7) (1997) 1863–1867.
[27] A.P. Goswami, L.K. Sachdeva, M.K. Mitra, G.C. Das, Relationship between short-crack fracture toughness and wear resistance of liquid-phase-sintered aluminas, to be presented in CFFGLACE-99, Calcutta, India, 22–23 September 1999.
[28] R.W. Davidge, T.J. Green, The strength of two-phase ceramic–glass materials, J. Mater. Sci. 3 (1968) 629.
[29] B.R. Lawn, Fracture of Brittle Solids, 2nd ed., Cambridge Solid State science series, pp. 194–206.
[30] M.I. Peterson, T.Y. Tien, Effect of the grain boundary thermal expansion co-efficient on the fracture toughness in silicon nitride, J. Am. Ceram. Soc. 78 (1995) 2345–2352.
[31] C.W. Li, J. Yamanis, Super-tough silicon nitride with R-curve behavior, Ceram. Eng. Sci. Proc. 10 (1989) 632–645.
[32] A.P. Goswami, G.C. Das, Role of fabrication route and sintering on wear and mechanical properties of liquid-phase-sintered alumina, Ceram. Int., submitted for publication.
[33] P.F. Becher, et al., Microstructural design of silicon nitride with improved fracture toughness: I. Effects of grain shape and size, J. Am. Ceram. Soc. 81 (1998) 2821–2830.